

# Topology optimization of periodic beam lattices using Cosserat elasticity

Gergely Molnár\*, Nawfal Blal

Univ Lyon, CNRS, INSA Lyon, LaMCoS, UMR5259, 69621 Villeurbanne, France



## ARTICLE INFO

### Article history:

Received 17 October 2022

Accepted 24 March 2023

### Keywords:

Cosserat elasticity  
Topology optimization  
Lattice structures  
Gradient elasticity  
Metamaterial

## ABSTRACT

This paper presents a novel method based on the Cosserat theory to optimize the topology of metamaterials made of slender beams. First, we filled the gap in the literature and compared the optimal topology of discrete Euler–Bernoulli beam lattices with counterparts obtained using the homogenized Cosserat theory. We investigated the effect of material and numerical parameters on the optimization results and the global stiffness. Finally, the paper highlights the importance of second-order models for slender lattice structures through different macroscopic geometries. For the first time, we presented an excellent quantitative agreement between continuum Cosserat and discrete beam results. We demonstrated that the Cosserat theory is necessary and sufficient to optimize slender, lightweight designs with lattice-based microstructures. Furthermore, the results showed that the locally allowed volume fraction was the most critical limiting parameter when maximizing global stiffness. Finally, we found that the reinforced honeycomb lattice is the stiffest microstructure for a given mass among the investigated forms.

© 2023 Elsevier Ltd. All rights reserved.

## 1. Introduction

Historically, when creating structures with large spans (e.g., bridges, roofs, or towers), lattice and truss elements were used to reduce the total mass and increase the global stiffness. However, early in history, structural engineers realized that by increasing the space between bent components, the added tensile and compression forces would increase the bending inertia quadratically with the distance (Huygens–Steiner theorem). As a consequence, the additional bending momentum would magnify not only the stiffness but also the global stability of the structures. This way, structures can span considerable distances that are not accessible to solid forms.

A similar phenomenon is seen in nature. A structural hierarchy is found when observing the microstructure of diverse load-bearing components. Examples range from cork [17], through many Diatom species [31], honeycombs [45], and the trabecular bone [36,51]. In all cases, smaller beam-like elements form an intricate network based on the characteristic loads.

In recent years, with the advancements in additive manufacturing, metamaterials with custom-made microstructures have been prepared [6]. In addition to an increased stiffness, this small-scale procedure makes the load-bearing elements stronger. Moreover, as the material approaches its microscopic length scale, the manufacturing defects' size and effect are reduced. As a result,

macroscopically brittle materials might behave in a ductile manner [74,8], thereby giving rise not only to a lightweight and stiff material but also a resistant one.

Thanks to the advanced manufacturing processes, developing new products with specific optimized properties is possible by modifying their shape or topology. Topology optimization provides a suitable mathematical framework to optimize the material distribution, i.e., the spatial distribution of the material in a design domain. After defining a cost function to be minimized, the sensitivity analysis provides an updating scheme for the design variables. The cost function can be defined for various quantities of interest (compliance, maximal stress, target shape, displacements, etc.). Topology optimization problems can be considered constrained as Partial Differential Equation (PDE) design problems, requiring a combination of optimization solvers and numerical discretization schemes to solve the PDEs physical equations (mainly the finite element method). Two types of optimization solvers can be used: (i) meta-heuristic approaches needing only a back run call of different cost function computations [20] and (ii) gradient-based solvers where the derivative of the cost function is required. Gradient-based topology optimization is usually based on the adjoint state method.

The literature cites several approaches for topology optimization. Density-based techniques pioneered by the standard Solid Isotropic Material with Penalization (SIMP) method [10,12] have proven their efficiency in structural topology design for a broad range of applications. SIMP considers density variables defined at each element of the finite element discretization as the optimized

\* Corresponding author.

E-mail address: [gergely.molnar@insa-lyon.fr](mailto:gergely.molnar@insa-lyon.fr) (G. Molnár).

topology's design parameters (design variables). The main idea is to consider the elastic behavior at each element designated by a power law introducing a density variable that has a value between 0 (no material) and 1 (material) and a power law parameter (larger than 1) aiming to penalize intermediate densities. Consequently, when the penalization parameter is adequately chosen, the spatial material distribution leads to an optimized structure with only two material types: void regions (elements with no stiffness) and solid regions (elements whose stiffnesses equal the bulk behavior). Empirically, the penalization parameters are taken to be greater than 3. However, the works of Bendsøe and Sigmund [11] propose a rigorous methodology for their calibration.

One other important issue when using such approaches is the checkerboard pathology. It is due to the apparition of neighboring elements with alternating void and solid materials. This problem can be addressed with the use of filter solutions. Usually, one can employ density filters to impose limitations on the density variation by a fixed length scale in the stiffness distribution. Another option is to introduce sensitivity filtering so that the design sensitivity is maintained in a fixed neighborhood. Filtering techniques are efficient for limiting mesh-dependency in density-based topology optimization solvers [13].

The other class of topology optimization is based on the level-set function as a parametrization of the design domain topology [57,48]. The level-set function represents the boundaries between void and solid phases, and the spatial evolution of the void-solid interfaces is usually governed by a shape derivative [60] or a topological derivative [30] to find the gradient direction toward the optimized topology. In recent years, numerous investigations have been proposed for level-set-based topology optimization approaches [4,3,68,46].

Thanks to the recent advent of manufacturing technologies, the design of advanced materials, incorporating small scales with complex topologies, has become possible. However, simulations for structural optimization describing the finest scales are computationally expensive. Therefore, multi-scale topology optimization techniques have emerged as a macro-to-micro optimization technique with noteworthy performances. The optimized structure results from the macro topology design as the optimized representation of ascribed microstructures (which can be spatially varying). Such two-scale optimization bridges the underlying scales with less expansive effort while capturing relevant microstructural effects. However, the optimization process considers the microstructure effect exclusively by its effective (homogenized) behavior. Various previous studies have investigated the potential macro-micro design optimization [38,32,29,72,66,27,56,71,64,43], and most of the corresponding papers are based on scale separation assumptions and periodic homogenization theory. In order to accelerate multi-scale processes, approaches merging data-driven techniques have recently been developed to accelerate multi-scale topology optimization solvers [22,67,34,73,21]. Furthermore, machine-learning and surrogate-based optimization techniques [7] could be extended to the topology optimization of materials with underlying microstructures.

The main explorations deal with the framework of the Cauchy theory, and the methods are thus suitable for large-scale transitions but limited to exhibiting the microstructure size effects. Moreover, such first-order frameworks fail when the scale separation assumption does not prevail (e.g., when topology cells are kinematically coupled as in some compliant mechanisms). Enriched kinematic homogenization schemes are needed to efficiently design architected materials and capture local microstructural effects, mutual interactions, non-localities, or instabilities.

One of the first higher-order theories was proposed by the Cosserat brothers [19]. They enriched the simple Cauchy model with

an independent rotation field gradient. This way, the model had three displacement and three rotational degrees of freedom (in 2D: two displacements DoFs and one rotation DoF). This theory was the first to define couple stresses and to render the Cauchy stress tensor non-symmetric. Since its first introduction, Toupin [63] formulated the energy density function using the classic displacement and rotation gradient terms. Finally, Mindlin [44] gave the linearized mathematical theory, serving as the basis of the variational solution.

Since its first introduction, the Cosserat theory has been used in numerous fields, such as granular materials [40], masonry structures [1], composites [35], or even human bone [37,47]. However, most importantly, it was shown that Cosserat elasticity efficiently captures the effect of the intrinsic length scale in cellular structures [54]. The constitutive equations of the model can be written in several forms ranging from a single added constant to Hooke's law [2] to the entirely redefined stiffness matrix [70]. However, one of the main disadvantages of the Cosserat theory is that it has too many material parameters.

Bottom-up homogenization methods are usually applied to determine the elastic Cosserat constants of lattice structures. Two main approaches exist: (i) the micro-scale is represented by an inhomogeneous Cauchy continuum [26,23,25,24], and (ii) the lattices are modeled with either Euler-Bernoulli [49,55,50] or Timoshenko-Ehrenfest beams [41]. The important difference is that in the latter case, the rotational degrees of freedom are already present at the microscale. On the other hand, with beam theory, the solid volume fraction cannot be represented. This paper focuses on analytical results obtained using the asymptotic method on Euler-Bernoulli beams [49,55], and the limitations of the model are discussed.

In recent years, various studies have been devoted to obtaining the optimal topology with a characteristic length scale by using the Cosserat theory. Most works have focused on fictitious materials with only a few elastic constants. Parameter studies have been conducted to investigate the effect of the intrinsic length [28,53,42,5,39], the fundamental eigenfrequencies [14,61,62], the Cosserat shear modulus [18], and even 3D non-centrosymmetry [65]. A majority of the investigations were based on the use of the SIMP and the level-set methods to obtain the results.

Among the various models proposed in the literature, second gradient elasticity (such as a Cosserat medium) and micromorphic [69,52] computational homogenization methods seem to be adequate tools to be integrated into topology optimization simulations. Indeed, encouraging recent results for bottom-up multi-scale modeling of microstructural materials with enriched kinematics revive their use in design optimization. However, this topic remains an open research field [15].

Most studies focusing on the topology optimization of the Cosserat medium use fictitious material parameters, whereas papers presenting the optimization of lattice structures calculate only the Cauchy coefficients [67]. A comparative analysis using real microstructures and a homogenized second-order continuum has yet to be performed.

Certain periodic beam lattices were shown to behave as the Cosserat continuum when properly homogenized. Due to the discrete network of the joints, an independent rotation can be defined. This is confirmed herein by topology optimization. In this paper, we present a new method to optimize the topology of slender lattice structures with small local volume fractions. We compare the optimal topology of discrete Euler-Bernoulli beam lattices to topologies obtained using the Cosserat theory. The local stiffness is calculated based on real geometrical properties, such as the beam height or the slenderness. We finally highlight the importance of the enriched model in the optimization of lattice

structures and present optimal microstructures for a variety of macroscopic mechanical problems.

The paper is structured as follows. First, Section 2 introduces the basic concept of topology optimization, after which Section 3 lays out the different mechanical descriptions. Subsequently, Section 4 discusses the effect of both numerical and lattice parameters on the optimal topology. This is followed by a discussion on the optimal microstructure in Section 5. Finally, Section 6 concludes the paper.

## 2. Topology optimization

Topology optimization is a design method in which the material is distributed inhomogeneously in the design domain to maximize a specific property. We chose to use the algorithm published by Sigmund [59] and replaced the arbitrary design variable with the height of the beams. Among its advantages, the modified algorithm is easy to implement, robust and converges rapidly. Despite that Bendsoe and Sigmund [11] showed that, for the SIMP method, the cubic penalty function is physically permissible, we decided to use the constitutive analytic relations. Based on the Bernoulli beam theory, the Cosserat stiffness constants used in this paper were deduced from asymptotic approaches [49,55]. In addition, constraints on the maximum height and volume ratios are discussed in Section 3.

The overall aim of the topology optimization procedure is to keep the compliance of the model at a minimum by minimizing the potential energy as a function of the local design variables:

$$\mathbf{h} = \underset{\mathbf{h}}{\text{Argmin}} \left\{ c(\mathbf{h}) = \frac{1}{2} \mathbf{U}^T \mathbf{K} \mathbf{U} = \frac{1}{2} \sum_{e=1}^N \mathbf{u}_e^T \mathbf{k}_e(h_e) \mathbf{u}_e \right\}. \quad (1)$$

This was done by respecting the equilibrium constraint:

$$\mathbf{K} \mathbf{U} = \mathbf{F}, \quad (2)$$

and the volume constraint:

$$\frac{V(\mathbf{h})}{V_0} = f, \quad (3)$$

with lower and upper bounds on the design variables (beam heights):

$$0 < \mathbf{h}_{\min} \leq \mathbf{h}_e \leq \mathbf{h}_{\max}. \quad (4)$$

In Eq. (1),  $c$  is the total potential energy,  $\mathbf{U}$  and  $\mathbf{u}_e$  are the vectors of the global and elementary degrees of freedom (translation, rotation),  $\mathbf{K}$  and  $\mathbf{k}_e$  are the global and elementary stiffness matrices,  $N$  is the number of finite elements in the design domain and  $\mathbf{h}$  is the vector containing the elementary design variables ( $h_e$ ). In our case, this is the height of the beam cross sections. In this paper, we assume rectangular beam sections with a unitary thickness in the out-of-plane ( $z$ ) direction. In the equilibrium Eq. (2),  $\mathbf{F}$  is the global force vector,  $V$  is the total volume of the model,  $V_0$  is the volume of the design domain, and  $f$  is called the relative density or prescribed volume fraction.

The optimization problem is formulated based on the algorithm proposed by Sigmund [59]. Apart from that work, the penalty exponent was replaced by the exact stiffness as a function of the beam height (the design variable); as in lattice structures, this variable comes with a physical meaning. The optimality criteria method [9] with a sensitivity filter [58] was utilized to update the design variables for a given equilibrium problem.

As shown in Fig. 1, we kept the original structure of Ref. [59]. However, we replaced each block with our own features. As the paper discusses different mechanical descriptions (Cauchy, Cosserat, Euler–Bernoulli beam) for the same mechanical problem, these blocks vary accordingly.

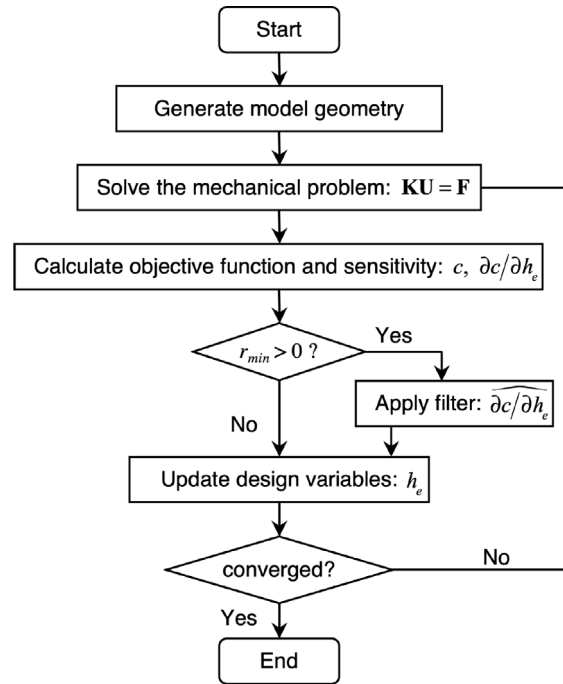


Fig. 1. Basic structure of the topology optimization algorithm.

First, the finite element model was generated, after which the first equilibrium was obtained. The analytic solutions were applied to calculate the stiffness, energy, and sensitivity functions. For the Cosserat medium, the results of references [49,55] were utilized. Finally, the filter was applied directly to the array containing the sensitivity functions, as initially done by Sigmund [59] where  $r_{\min}$  was the effective filter distance. Next, the design variables were updated iteratively to satisfy the volume constraint. Finally, the convergence was verified: if the maximum change in the design variable was smaller than  $(h_{\max} - h_{\min})/1000$ , the algorithm was stopped. Otherwise, a new equilibrium was determined with the new design variable distribution. A maximum number of 200 iterations were allowed by default. However, the objective function was monitored continuously. The optimization procedure continued if the change in potential energy had not converged.

## 3. Mechanical description

This section briefly summarizes the basic mechanical descriptions used in the paper. All simulations assumed a static equilibrium, wherefore each model was governed by a set of equations describing equilibrium, the kinetic constraints, and the material model.

### 3.1. Cauchy continuum

In continuum mechanics, probably one of the most frequently used assumptions is proposed by Cauchy [16]. The equilibrium of the differential object is depicted in Fig. 2a) and can be described with the following set of equations:

$$\begin{aligned} \nabla \cdot \boldsymbol{\sigma} + \mathbf{b} &= \mathbf{0} & \text{in } \Omega, \\ \boldsymbol{\sigma} \cdot \mathbf{n} &= \bar{\mathbf{t}} & \text{on } \Gamma_N, \\ \mathbf{u} &= \bar{\mathbf{u}} & \text{on } \Gamma_D, \end{aligned} \quad (5)$$

where  $\boldsymbol{\sigma}$  is the stress tensor, and  $\mathbf{b}$  represents body forces (in our case, zero). The second and third rows describe, respectively Neu-

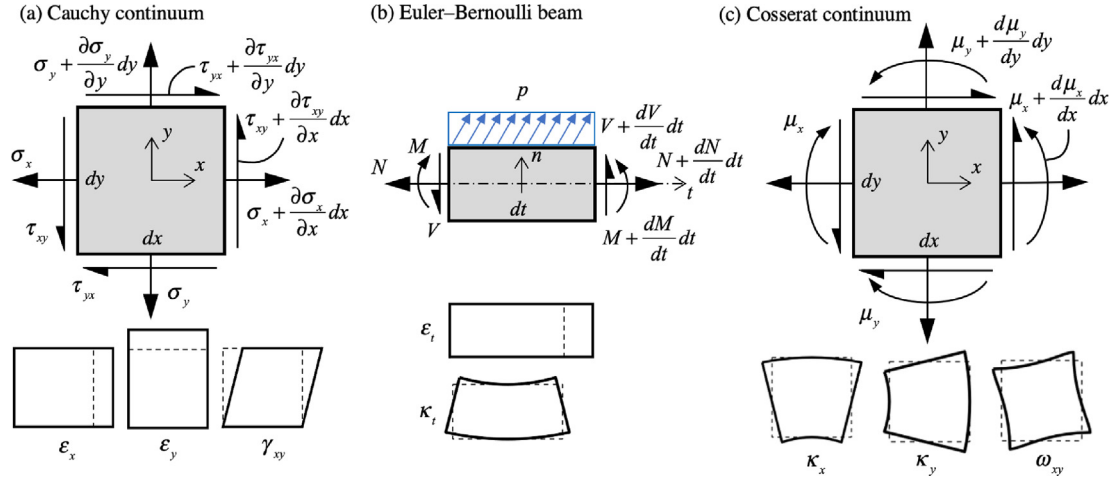


Fig. 2. Equilibrium and admissible deformations of the elementary volume of the (a) Cauchy, (b) Euler-Bernoulli beam, and (c) Cosserat theories.

mann and Dirichlet boundary conditions. The bar symbol represents external forces ( $\bar{\mathbf{t}}$ ), and prescribed displacements ( $\bar{\mathbf{u}}$ ).

The material is considered to be linear elastic:

$$\boldsymbol{\sigma} = \mathbf{C}\boldsymbol{\varepsilon}, \quad (6)$$

where  $\mathbf{C}$  is the stiffness matrix and  $\boldsymbol{\varepsilon}$  the strain tensor. Due to the local equilibrium ( $\sigma_{xy} = \sigma_{yx} = \tau_{xy}$ ) the Voight notation can be used, thus simplifying the stress tensor to a vector with 3 components in 2D:  $\boldsymbol{\sigma} = [\sigma_x \ \sigma_y \ \tau_{xy}]^T$ . Consequently,  $\mathbf{C}$  becomes a  $3 \times 3$  matrix. The strain tensor is also simplified to the three elementary deformations shown in Fig. 2(a). Assuming small deformations, the displacement-strain relationship can be expressed as:

$$\varepsilon_x = \frac{\partial u_x}{\partial x}, \varepsilon_y = \frac{\partial u_y}{\partial y}, \gamma_{xy} = \frac{\partial u_x}{\partial y} + \frac{\partial u_y}{\partial x}. \quad (7)$$

To solve the mechanical problem, the following energy is minimized with respect to the degrees of freedom by following the kinematically admissible set given in Eq. (5)<sub>3</sub>. In this first case, the displacements are obtained by solving the following minimization problem:

$$\mathbf{u} = \text{Arginf}_{\mathbf{u}} \left\{ \int_{\Omega} \frac{1}{2} \boldsymbol{\varepsilon}^T \mathbf{C} \boldsymbol{\varepsilon} - \mathbf{b} \cdot \mathbf{u} d\Omega - \int_{\Gamma} \bar{\mathbf{t}} \cdot \mathbf{u} d\Gamma \right\}. \quad (8)$$

### 3.2. Euler-Bernoulli model

To model slender beam structures, the Euler-Bernoulli beam theory provides the most approachable framework. The classical beam theory is adapted to describe the behavior of elongated load-bearing elements with one side significantly larger than the others. The three primary assumptions that have to be made are that (i) the plane sections remain plane, (ii) the plane sections are perpendicular to the neutral axis, and (iii) the deformed beam angles are small. Thus, the equilibrium shown in Fig. 2(b) can be described by the following equations:

$$\begin{aligned} \frac{d^2 M}{dt^2} + p_n &= 0, \\ \frac{dN}{dt} + p_t &= 0. \end{aligned} \quad (9)$$

Here,  $M$  and  $N$  represent the bending moment and the normal force, and  $p_n$  and  $p_t$  are distributed loads perpendicular and parallel to the neutral axis. These equations are completed with Neumann and Dirichlet boundary conditions similar to that of Eq. (5)<sub>2,3</sub>. The Euler-Bernoulli beam theory neglects the effect of shear deformation, and as a result, it is adapted to describe the response of slender beams. The linear elastic response can be obtained by:

$$\begin{aligned} M &= EI\kappa_t, \\ N &= EA\varepsilon_t, \end{aligned} \quad (10)$$

where  $\kappa_t$  and  $\varepsilon_t$  are the two types of deformations present beams can be subjected to: (i) curvature/bending and (ii) elongation/compression.  $E$  is Young's modulus,  $I$  is the bending moment of inertia around axis  $z$ , and  $A$  is the area of the cross-section.

To obtain the relationship between the degrees of freedom and the deformations, the following assumptions are used:

$$\kappa_t = \frac{\partial \phi}{\partial t} = \frac{\partial^2 u_n}{\partial t^2}, \quad \varepsilon_t = \frac{\partial u_t}{\partial t}, \quad (11)$$

where  $\phi$  is the rotation,  $u_n$  is the perpendicular displacement, and  $u_t$  is the parallel displacement in relation to the neutral axis.

To obtain equilibrium, the following energy functional is minimized by following the kinematically admissible set:

$$(\mathbf{u}, \phi) = \text{Arginf}_{\mathbf{u}, \phi} \left\{ \int_L \frac{1}{2} (\varepsilon_t^2 EA + \kappa_t^2 EI) dL - \mathbf{p} \cdot \mathbf{u} dL - \bar{\mathbf{t}} \cdot \mathbf{u} - \bar{M} \cdot \phi \right\}. \quad (12)$$

The bar symbol represents external forces ( $\bar{\mathbf{t}}$ ), and moments ( $\bar{M}$ ).

### 3.3. Cosserat continuum

The classical description of continuum mechanics is ill-suited to characterize the response of materials with an inhomogeneous microstructure, *i.e.*, a characteristic microscopic length scale. However, the mechanical behavior of architected materials (*e.g.*, lattice structures) is often determined by their specific micro-scale configurations. Therefore, the Cosserat theory (or micropolar elasticity) incorporates rotational degrees of freedom ( $\phi$ ) into the mechanical description.

The Cauchy model is completed with an additional set of equations describing momentum equilibrium, as shown in Fig. 2(c):

$$\begin{aligned} \nabla \cdot \boldsymbol{\sigma} + \mathbf{b} &= \mathbf{0} & \text{in } \Omega, \\ \nabla \cdot \boldsymbol{\mu} + \boldsymbol{\sigma} \hat{\mathbf{e}} &= \mathbf{0} & \text{in } \Omega, \\ \boldsymbol{\sigma} \cdot \mathbf{n} &= \bar{\mathbf{t}} & \text{on } \Gamma_N, \\ \boldsymbol{\mu} \cdot \mathbf{n} &= \bar{M} & \text{on } \Gamma_N, \\ \mathbf{u} &= \bar{\mathbf{u}} & \text{on } \Gamma_D, \\ \phi &= \bar{\phi} & \text{on } \Gamma_D. \end{aligned} \quad (13)$$

In this equation,  $\sigma$  is now a non-symmetric ( $\sigma_{xy} \neq \sigma_{yx}$ ) force-stress tensor,  $\mu$  is the moment or couple-stress tensor, and  $\tilde{\epsilon}$  is the Levi-Civita symbol. The bar symbol represents external forces ( $\bar{\mathbf{f}}$ ), moments ( $\bar{\mathbf{M}}$ ), prescribed displacements ( $\bar{\mathbf{u}}$ ), and rotations ( $\bar{\phi}$ ).

The literature [25] recounts various ways to define linear elastic behavior. In this paper, we chose to correlate the complete stress tensor to the deformation components using the following model:

$$\begin{bmatrix} \sigma_x \\ \sigma_y \\ \tau_{xy} = \frac{\sigma_{xy} + \sigma_{yx}}{2} \\ \vartheta_{xy} = \frac{\sigma_{xy} - \sigma_{yx}}{2} \\ \mu_x \\ \mu_y \end{bmatrix} = \begin{bmatrix} [\mathbf{C}]_{3 \times 3} & \mathbf{0} & \mathbf{0} \\ \mathbf{0} & G_c & \mathbf{0} \\ \mathbf{0} & \mathbf{0} & [\mathbf{D}]_{2 \times 2} \end{bmatrix} \begin{bmatrix} \epsilon_x \\ \epsilon_y \\ \gamma_{xy} \\ \omega_{xy} \\ \kappa_x \\ \kappa_y \end{bmatrix} \quad (14)$$

As a result, the first three elements of the stress vector correspond to the Cauchy stress components, the fourth element provides the difference between  $\sigma_{xy}$  and  $\sigma_{yx}$ , and finally, the last components are the couple stresses.

The corresponding deformations are depicted in Fig. 2(c), with the missing kinematic constraints described by the following:

$$\omega_{xy} = \frac{\partial u_x}{\partial y} - \frac{\partial u_y}{\partial x} - 2\phi, \quad \kappa_x = \frac{\partial \phi_x}{\partial x}, \quad \kappa_y = \frac{\partial \phi_y}{\partial y} \quad (15)$$

The equilibrium is then obtained by minimizing the following functional equations:

$$(\mathbf{u}, \phi) = \text{Arginf}_{\mathbf{u}, \phi} \left\{ \int_{\Omega} \frac{1}{2} [\mathbf{e}^T \mathbf{C} \mathbf{e} + \omega_{xy}^2 G_c + \boldsymbol{\kappa}^T \mathbf{D} \boldsymbol{\kappa}] - \mathbf{b} \cdot \mathbf{u} d\Omega - \int_{\Gamma} \bar{\mathbf{t}} \cdot \mathbf{u} + \bar{m} \cdot \phi d\Gamma \right\} \quad (16)$$

By incorporating rotational degrees of freedom into the continuum description, the Cosserat theory proposes an analogous description to the discrete beam model with a significantly lower computational cost.

### 4. Numerical examples

Fig. 3(a) depicts the geometry of the optimization problem. In this section, a cantilever geometry of length ( $L$ ) 100 and height ( $H$ ) 50 was chosen. The concentrated force ( $F$ ) applied at the end was  $10^{-3}$  unless otherwise specified. In the first two subsections, the continuum meshes were chosen identically. Therefore, the effect of the concentrated load on the results was negligible. When comparing different mesh sizes, the concentrated force was replaced by boundary traction. This paper presents the model and the results in dimensionless quantities. Young's modulus was set to 1. Both translational and rotational degrees of freedom were constrained on the nodes on the left side.

For a beam structure, the volume constraint, defined in Eq. (3) can be expressed by summing up all the individual elements and dividing the sum by the overall area of the design domain:

$$f = \frac{V(\mathbf{h})}{V_0} = \frac{\sum_{e=1}^N h_e l_e}{LH} \quad (17)$$

where  $V_0$  is the total volume of the design domain,  $l_e$  represents the individual length of the beams, and  $h_e$  is their height. There are  $N$  beams in the structure. In this case,  $h_e$ , The design variable has a geometrical significance wherefore its bounds can be defined as:

$$0 < h_{\min} \leq h_e \leq h_{\max} \quad (18)$$

with  $h_{\min}$  as a lower bound responsible for numerical stability ( $h_{\min} = h_{\max}/5000$ ), and  $h_{\max}$  as an upper bound:

$$h_{\max} \leq \frac{V_0}{\sum_{i=1}^N l_i} \quad (19)$$

The characteristic quantities, upper bounds, and the correlation between local volume fraction and beam height are summarized in Table 1.

When using  $h_{\max}$ , the RVE should be considered solid ( $f_{\text{RVE}} = 1$ ). This limit is unsuitable for beam theory, and consequently, in the following examples,  $h_{\max}$  is set to  $l_e/5$ , at which value the Euler-Bernoulli beam theory still gives a fairly precise outcome (the difference to the Timoshenko-Ehrenfest theory is 3.06%).

Part (b) of Fig. 3 shows the optimization results of a rectangular lattice modeled using the Cauchy continuum (with SIMP) and Euler-Bernoulli beams. When employing the Cauchy description, the design variable was penalized using a cubic function, and the maximum value of the design variable was limited to 0.4, which corresponds to the volume ratio of the rectangular grid RVE when  $h_e = l_m/5$ . It can be clearly seen that Cauchy's description with the SIMP technique is unable to correctly determine the optimal topology.

In the present paper, we discuss three microstructures: square, hexagonal, and reinforced honeycomb lattices. The reason for this is that the analytic Cosserat stiffness components for these structures are available in the literature [49,55]. Tables 2 and 3 summarize each constant of the matrices  $\mathbf{C}$ ,  $\mathbf{D}$ , and the component  $G_c$ . The remaining components of the matrices were zero.

The aim of Section 4 is to prove that the Cosserat medium is necessary and sufficient to optimize the topology of light and slender beam lattices. Therefore, each material and numerical parameter was tested using the Euler-Bernoulli beam and the Cosserat theory, after which the optimal topology and the final displacement ( $u_y^f$ ) measured at the concentrated force  $F$  were compared. It should be noted that the objective function (potential energy) was equal to  $c = Fu_y^f/2$ , and the potential energy was thus not an independent measure of optimality.

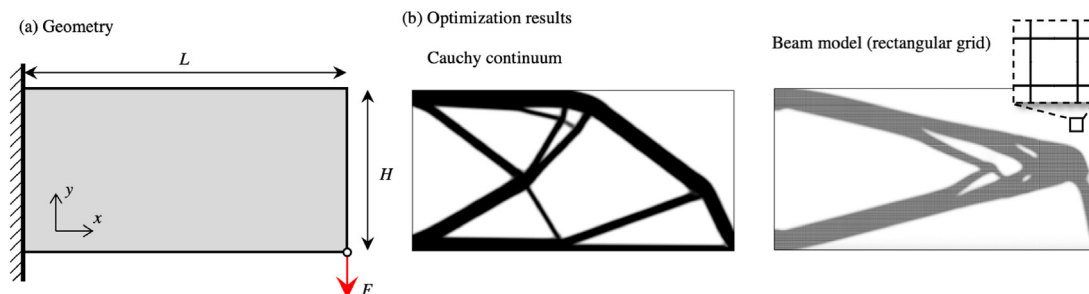


Fig. 3. Optimized topology of a cantilever: (a) geometry ( $L = 100, H = 50$ ), (b) optimal topology using the Cauchy and the beam model for  $f = 0.12$  ( $r_{\min} = 1$ ).

**Table 1**  
Lattice geometries and correlation between volume ratio and beam height.

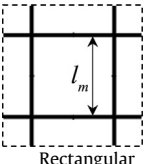
Lattice type	$l_x$	$l_y$	$\sum l_e$	$V_{RVE}$	$h(f_{RVE})$	$f_{RVE}(h)$	$f_{RVE}(l_e/h = 5)$
Rectangular	$l_m$	$l_m$	$2l_m$	$l_m^2$	$\frac{l_m f_{RVE}}{2}$	$\frac{2h}{l_m}$	0.4
Honeycomb	$\sqrt{3}l_m$	$3l_m$	$6l_m$	$3\sqrt{3}l_m^2$	$\frac{\sqrt{3}}{2}l_m f_{RVE}$	$\frac{2h}{\sqrt{3}l_m}$	$\frac{2}{5\sqrt{3}} = 0.23$
Reinforced honeycomb	$\sqrt{3}l_m$	$3l_m$	$l_m(6 + 6\sqrt{3})$	$3\sqrt{3}l_m^2$	$\frac{\sqrt{3}l_m f_{RVE}}{2+2\sqrt{3}}$	$\frac{h}{l_m} \frac{2+2\sqrt{3}}{\sqrt{3}}$	$\frac{2+2\sqrt{3}}{5\sqrt{3}} = 0.63$

4.1. Square lattice

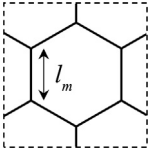
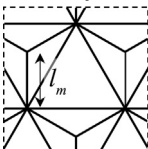
The homogenized stiffness of a rectangular grid lattice is orthotropic. The two principal orientations are parallel to the two main beam directions. Due to the lack of normal interaction,  $C_{12} = 0$ , which means that extension in one direction causes no contraction in the other. This property signifies that the homogenized material's Poisson's ratio is zero ( $\nu = 0$ ). The rectangular beam lattice was used to demonstrate the effect of the volume fractions on the optimal topology. We distinguish between local  $f_{RVE}$  and global  $f$  values, where  $f_{RVE}$  represents the allowed maximum local volume fraction, while  $f$  is the global volume fraction defined in Eq. (17). These two quantities are independent, with  $f \leq f_{RVE}$ , and  $f_{RVE}$  is mostly controlled by prescribing a lower beam height in the model based on the correlation shown in Table 1. Due to the difference in local geometry, various lattice structures have different  $f_{RVE}$  for the same  $l_e/h_e$  ratio.

The beam model was constructed from  $300 \times 150$  RVEs. The beam segments were unified, which resulted in 90 450 beam finite elements with  $l_m = 1/3$ . The load was applied on a node situated on the bottom line furthest to the right. The Cosserat model was divided into  $300 \times 150$  4-node quadrilateral elements. We used 45000 elements to capture similar topology details as in the beam model. The advantage of the Cosserat model is that  $l_m$  reduces to a material parameter, and the element size does not affect it. The material and the boundary conditions can be found in the main part of Section 4. A filter of  $r_{min} = 1$  was used in both cases.

**Table 2**  
Cosserat constants for the rectangular beam lattice [55].

Lattice type	$C_{11}, C_{22}$	$C_{12}, C_{21}$	$C_{33}$	$G_c$	$D_{11}, D_{22}$
	$\frac{ht}{l_m} E$	0	$\frac{th^3}{2l_m^3} E$	$\frac{th^3}{2l_m^3} E$	$\frac{th^3}{12l_m^3} E$

**Table 3**  
Cosserat constants for honeycomb and reinforced honeycomb beam lattices [49].  $C_{11} = C_{22} = K_s + G_s, C_{12} = C_{21} = K_s - G_s, C_{33} = G_s$ .

Lattice type	$K_s$	$G_s$	$G_c$	$D_{11}, D_{22}$
	$\frac{\sqrt{3}}{6} \frac{Eth}{l_m}$	$\frac{Eth^3}{\sqrt{3}l_m(l_m^2+h^2)}$	$\frac{Eth^3}{2\sqrt{3}l_m^3}$	$\frac{Eth^3}{12\sqrt{3}l_m^3}$
	$\frac{3+\sqrt{3}}{6} \frac{Eth}{l_m}$	$\frac{l_m^6 + 4(\sqrt{3}+1)l_m^4 l_m^2 + l_m^2 h^4}{4l_m^2(l_m^2+th^3)} E$	$\frac{3+\sqrt{3}}{6\sqrt{3}} \frac{Eth^3}{l_m^3}$	$\frac{1+\sqrt{3}}{12\sqrt{3}} \frac{Eth^3}{l_m^3}$

The first two rows of Fig. 4(a) and (b) show the optimal topology for two global volume fractions obtained using a beam model (left) and the Cosserat continuum (right). The third row portrays the change if thicker beams are allowed. The results displayed in the two columns are almost identical. However, they differed significantly from the outcome obtained using the Cauchy continuum and the SIMP technique shown in Fig. 3(b).

Similar to the topologies, the displacement results were also in good correspondence. Fig. 4(c) shows the effect of the local slenderness. The maximum difference between the deflection values was 2.16%, which was within the precision of the built models. Furthermore, we observed a tendency to favor thicker beams. When  $f_{RVE}$  increased, the maximum deflection decreased. Without a global stability analysis, the optimal topology favors thinner elements with higher local volume fractions. When  $h_{max}$  was reduced, the size of the global elements grew, raising the moment of inertia but lowering the leverage—resulting in a less rigid structure. This effect was demonstrated but not discussed by Watts [67], where the optimal topology was fairly independent of the chosen structure, and local maxima gave mostly solid parts (with  $f_{RVE} = 1$ ). Of course, this solution defeats the purpose of creating an architected material.

Finally, Fig. 4(d) presents a plot of the deflection results as a function of the global volume fraction with  $h_{max} = l_m/5$  ( $f_{RVE} = 0.4$ ). The results were fitted perfectly using a hyperbolic function. Moreover, the maximum difference was 3.8%, which demonstrated how well the Cosserat theory reproduced the mechanical response of these periodic beam structures.

4.2. Honeycomb lattice

In contrast, the homogenization of honeycomb lattices gives an isotropic response with a Poisson's ratio depending on the slenderness varying between 0.3–0.5 (for  $l_e/h_e = 5$ , it is 0.46). Therefore, as shown in Fig. 5, the optimal topologies are much closer to the results produced by SIMP. This section thus describes the use of the honeycomb structure to demonstrate the effect of the filter width ( $r_{min}$  on the topology and the maximum deflection at the concentrated force as a measure of optimality).

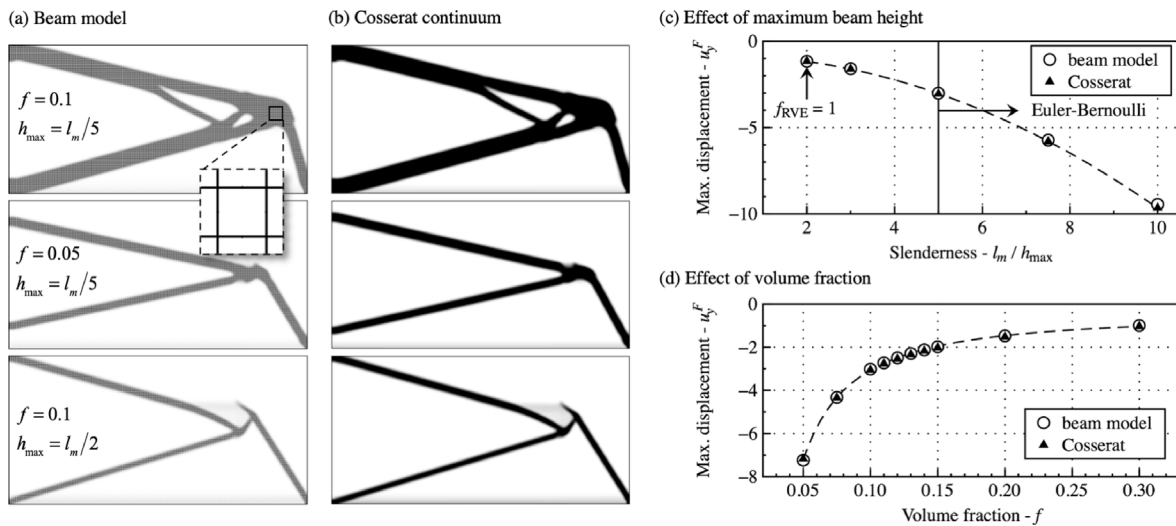


Fig. 4. Topology and deflection results on a rectangular grid as a function of local and global volume fractions.

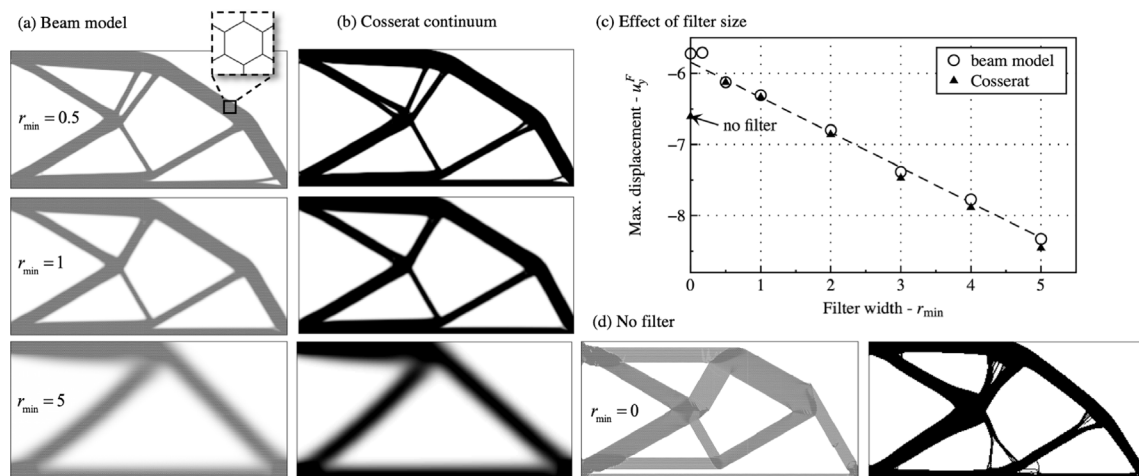


Fig. 5. Topology and deflection results on a honeycomb structure as a function of the filter width.

The beam model was constructed from  $300 \times 87$  RVEs. The beam segments were unified, which resulted in 156 387 beam finite elements with  $l_m = 0.192$ . The load was applied on a node situated on the bottom line furthest to the right. The Cosserat model was divided into  $300 \times 150$  4-node quadrilateral elements (45000 elements), similar to the rectangular case. The material and the boundary conditions can be found in the main part of Section 4. The filter width was varied throughout the analysis.

Fig. 5(a) and (b) show the results obtained using Euler–Bernoulli beams and the Cosserat continuum, respectively. An agreement was observed, highlighting the Cosserat theory’s versatile potential. When the filtering was switched off, as shown in Fig. 5(d). However, it is our opinion that these results bear little practical importance.

Finally, we plotted the maximum deflection in Fig. 5(c). Introducing the filter reduced the optimality and the overall stiffness of the structure. By increasing the filter width, the displacement increased linearly. However, when  $r_{min}$  was smaller than the shortest distance between the beam elements, the filter could no longer complete its task, and the results started to fluctuate. Until that point, the maximum difference between the two methods was 1.51%.

### 4.3. Reinforced honeycomb lattice

Our third example focuses on the effect of the characteristic micro length scale on the reinforced honeycomb network. In this case, the classic hexagonal structure was fortified with a triangular grid. While the hexagonal structure was mostly a bending-dominated lattice, triangular cells provided normal rigidity. The homogenized Cauchy stiffness was isotropic with a Poisson’s ratio varying between 0.3–0.34 (for  $l_e/h_e = 5$ , it is 0.325).

Different beam structures were created to test the effect of the micro-length. However, only whole RVEs were used to create the beam models. Due to the irrational size of the RVE, not many configurations had precisely the same size. Therefore, the following sample sizes were considered:  $142 \times 41$ ,  $239 \times 69$ ,  $284 \times 82$ ,  $336$  and  $426 \times 123$ , which corresponded to  $l_m = 0.4, 0.24, 0.2, 0.17$  and  $0.14$ , respectively.

The advantage of the Cosserat model is that there is no need to change the mesh for a different  $l_m$  value, as it is only a material parameter. However, both models were tested with a mesh following the change of  $l_m$  and one independent constant of  $300 \times 150$  elements.

The finite element mesh was generated from 4 node quadrilateral elements. The material and the Dirichlet boundary conditions can be found in the main part of Section 4. A filter of  $r_{\min} = 1$  was used in both cases.

After initial testing, the results showed that the concentrated force and the changing mesh had more significant effects on the deflection than  $l_m$ . Therefore, a model was developed to distribute the loading on a unit length. Practically, the force was divided and applied on the beam and the continuum model, as shown in Fig. 6.

Fig. 6(a) and (b) show that neither  $l_m$  nor the Neumann boundary affected the optimal topology. Both the beam and Cosserat models gave a solid-like outer shell (with  $f_{RVE}$ ) and a less filled interior. Fig. 6(c) displays the deflection results as a function of  $l_m$ . Its effect was found to be much smaller than the increased deflection originating from the singularity. When the load was distributed, a small increase in rigidity was observed in favor of larger motifs.

### 5. Discussion

In Section 4, we demonstrated that the Cosserat description was sufficient not only qualitatively but also quantitatively to describe the mechanical behavior of beam lattice structures. Moreover, the response, as well as the optimal topologies, was found to be in agreement. Due to the overall reduction in element number, the calculations were significantly accelerated using the continuum model. The calculations were executed on a personal computer with a 2.7 GHz Intel Core i7 processor using a single core. On average, the optimization process took 4-8 h for the beam models and 1 h for the continuum simulations.

Here, we take a step back to understand the critical components of the Cosserat description, ultimately investigating different structures (design domains) with varying  $L/H$  ratios to identify an "ideal" microstructure.

Fig. 7 shows the optimization problem introduced in Section 4. The elementary grid is a rectangular lattice with  $300 \times 150$  RVEs,

and the global volume fraction was set to  $f = 0.12$  with an  $r_{\min} = 1$  filter width. The results were compared with those of the beam model shown in Fig. 3(b).

Fig. 7(a) presents the optimal topology using the SIMP method with a  $\nu = 0$  material and a cubic penalty. In this first case, no limit was applied to the local volume ratio ( $f_{RVE} = 1$ ), and as a result, the final topology differed significantly from the results obtained as compared to the beam lattice. Furthermore, the deflection was much smaller because of the higher local volume ratio. As a result, the SIMP method with an isotropic material was inadequate to model slender lattice structures. In part (b) the maximum stiffness was calculated with  $f_{RVE} = 0.4$  based on Tables 1 and 2. To scale between empty and solid states, a cubic penalty was applied. This modification was the first step when the form started to resemble the results obtained with the beam model. The global form was recovered, however, the details remained dissimilar. Part (c) portrays the results when the penalty was omitted, and the stiffness was calculated based on 2. The details started to emerge, however, the deflection values overestimated the beam results ( $u_y^f = 2.5$ ) by 7.2%. Finally, part (d) presents the optimal topology obtained using the Cosserat theory. The details were fully recovered with a 1.2% difference in the deflation value.

The introduction of the rotational degree of freedom and the Cosserat theory clearly helped recover the finer details and the precise mechanical response of the underlying beam structures. Compared to the classical continuum, the finite element implementation of the theory was not much more complicated. The only difficulty lies in determining the Cosserat constants for arbitrary beam structures. However, this can be done using various homogenization methods [26,33,41]. The Cosserat optimization code used in this paper is included in Supplementary Materials.

The aspect ratio of the design space was varied to compare the three lattice structures. We were interested in determining whether an optimal microstructure could be found as a function of the geometry. According to Fig. 4(c), the locally allowed maximum volume fraction had a significant effect on the deflection

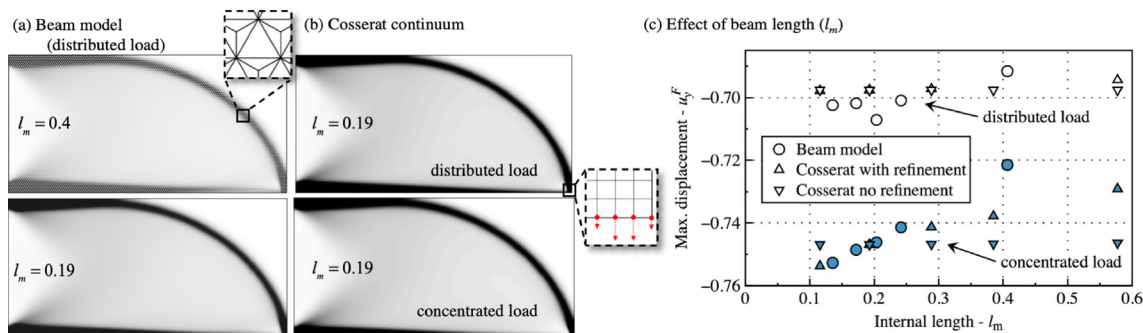


Fig. 6. Topology and deflection results on a reinforced honeycomb structure as a function of  $l_m$ . The results for the concentrated force are shown with solid symbols, whereas for the empty ones, the load was distributed on a unit length.

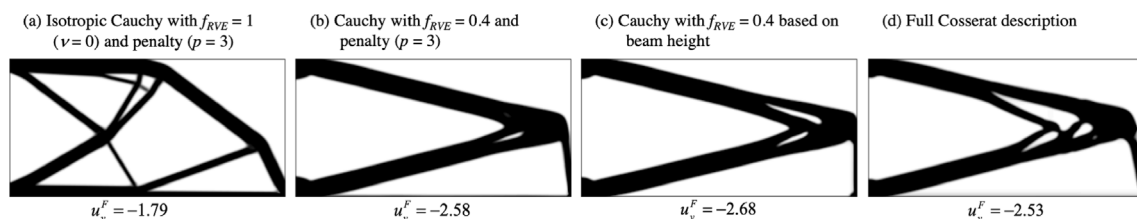
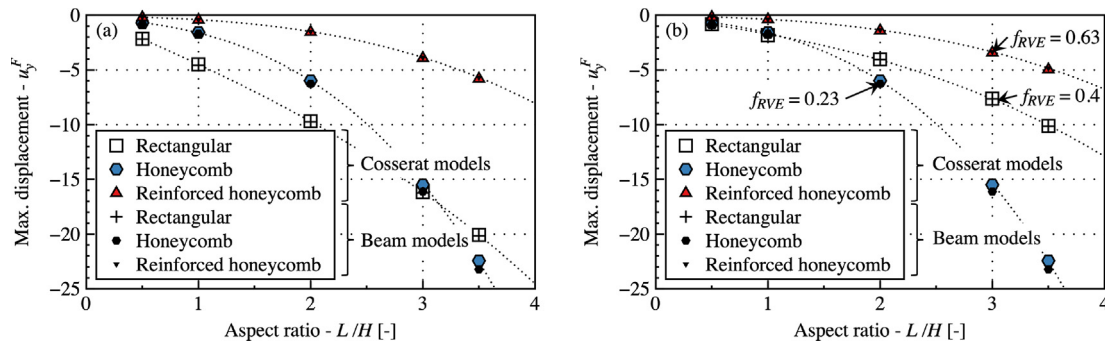


Fig. 7. Different approximations of the rectangular grid with the global volume ratio of  $f = 0.12$ : (a) isotropic Cauchy model with a maximum of  $f_{RVE} = 1$  and a cubic penalty; (b) Cauchy model with a maximum of  $f_{RVE} = 0.4$  and a cubic penalty; (c) Cauchy model with a maximum of  $f_{RVE} = 0.4$  based on the beam heights; (d) full Cosserat description. The rigidity was calculated based on Tables 2 and 3. The maximum displacement for the reference beam model at the concentrated load was  $u_y^f = -2.50$  (see topology result in Fig. 3).



**Fig. 8.** Maximum displacement as a function of the design space's aspect ratio for a global volume ratio of  $f = 0.075$  and  $l_m = 1/3$ : (a) with  $f_{RVE} = 0.23$  for all lattice geometries; (b) with their maximum volume ratios by respecting  $l_c/h_e \geq 5$ .

results. Therefore, in Fig. 8(a), we first compared results using the same local filling ratio,  $f_{RVE} = 0.23$ . Interestingly, there was a competition between the honeycomb and the rectangular grid. However, the reinforced honeycomb was consistently more rigid. When the local volume fraction of the rectangular grid was increased to 0.4, it became superior to the honeycomb, even in the initial interval. The results obtained using the Cosserat theory repeatedly corresponded well to the beam models. It could thus be stated that, depending on the design problem, the optimal RVE can be appropriately chosen using Cosserat elasticity.

## 6. Conclusion

This paper presents a topology optimization algorithm based on the Cosserat theory. The continuum results were compared and verified using Euler–Bernoulli beam models, and the stiffness of the enriched medium was determined from analytic calculations. We have carried out a systematic comparison between discrete beam and continuum simulations to validate the results of the latter method. This study fills the missing gap in the literature to show how continuum theory can be used in the optimization of architected materials.

We observed an excellent quantitative correspondence between continuum Cosserat and discrete beam results. We showed that the Cosserat theory was necessary and sufficient to optimize slender, lightweight designs with beam microstructures, and that the maximum local volume ratio (thus the maximum beam height) significantly affected the optimal deflection values. The effect of the filter width and the local length scale were also tested.

The addition of the rotational degree of freedom allowed us to capture the equivalent behavior of the beam theory. The advantage of the Cosserat model is that  $l_m$  reduces to a material parameter; therefore, the element size does not affect the microstructure. Consequently, the calculations can be significantly accelerated compared to beam models.

While the finite element implementation of the Cosserat theory is relatively simple, the stiffness components are available analytically only for a few periodic microstructures. Consequently, developing and publishing a universal homogenization algorithm is crucial in order to establish a database with various lattice structures used in practice. Furthermore, the algorithm should be employed to optimize the beam heights and, for example, the microscopic length scale.

## Data availability

The code and data used in the paper is published as a supplementary file.

## Declaration of Competing Interest

The authors declare that they have no known competing financial interests or personal relationships that could have appeared to influence the work reported in this paper.

## Appendix A. Supplementary material

Supplementary data associated with this article can be found, in the online version, at <https://doi.org/10.1016/j.compstruc.2023.107037>.

## References

- [1] Addressi D, Sacco E, Paolone A. Cosserat model for periodic masonry deduced by nonlinear homogenization. *Eur J Mech A Solids* 2010;29(4):724–37.
- [2] Aifantis EC. On the microstructural origin of certain inelastic models. *J Eng Mater Technol* 1984;106(4):326–30.
- [3] Allaire G, De Gournay F, Jouve F, Toader A-M. Structural optimization using topological and shape sensitivity via a level set method. *Control Cybernet* 2005;34(1):59.
- [4] Allaire G, Jouve F, Toader A-M. Structural optimization using sensitivity analysis and a level-set method. *J Comput Phys* 2004;194(1):363–93.
- [5] Arimitsu Y, Karasu K, Wu Z, Sogabe Y. Optimal topologies in structural design of micropolar materials. *Procedia Eng* 2011;10:1633–8.
- [6] Askari M, Hutchins DA, Thomas PJ, Astolfi L, Watson RL, Abdi M, et al. Additive manufacturing of metamaterials: A review. *Additive Manuf* 2020;36:101562.
- [7] Bacigalupo A, Gnecco G, Lepidi M, Gambarotta L. Computational design of innovative mechanical metafilters via adaptive surrogate-based optimization. *Comput Methods Appl Mech Eng* 2021;375:113623.
- [8] Bauer J, Schroer A, Schwaiger R, Kraft O. Approaching theoretical strength in glassy carbon nanolattices. *Nat Mater* 2016;15(4):438–43.
- [9] Bendsøe MP. Optimization of structural topology, shape, and material, vol. 414. Springer; 1995.
- [10] Bendsøe MP, Kikuchi N. Generating optimal topologies in structural design using a homogenization method. *Comput Methods Appl Mech Eng* 1988;71(2):197–224.
- [11] Bendsøe MP, Sigmund O. Material interpolation schemes in topology optimization. *Arch Appl Mech* 1999;69(9):635–54.
- [12] Bendsøe MP, Sigmund O. Topology optimization: theory, methods and applications. Springer; 2003.
- [13] Bourdin B. Filters in topology optimization. *Int J Numer Meth Eng* 2001;50:2143–58.
- [14] Bruggi M, Taliervo A. Maximization of the fundamental eigenfrequency of micropolar solids through topology optimization. *Struct Multidiscip Optim* 2012;46(4):549–60.
- [15] Calisti V, Lebée A, Novotny A, Sokolowski J. Sensitivity of the second order homogenized elasticity tensor to topological microstructural change. *J Elast* 2021;144:141–67.
- [16] Cauchy AL. Recherches sur l'équilibre et le mouvement intérieur des corps solides ou fluides, élastiques ou non élastiques. *Bull de la Société Philomat* 1823:9–13.
- [17] Chen B, Yuan Q, Luo J, Fan JH. Fibre reinforced cellular microstructure of cork wood. *Plast Rubber Compos* 2010;39(2):86–90.
- [18] Chen L, Wan J, Chu X, Liu H. Parameterized level set method for structural topology optimization based on the cosserat elasticity. *Acta Mech Sin* 2021;37(4):620–30.
- [19] Cosserat E, Cosserat F. Théorie des corps déformables. Librairie Scientifique A. Hermann et Fils; 1909.

- [20] Di Cesare N, Domaszewski M. A new hybrid topology optimization method based on i-pr-pso and eso. application to continuum structural mechanics. *Comput Struct* 2019;212:311–26.
- [21] Djourachkovitch T, Blal N, Hamila N, Gravouil A. Multiscale topology optimization of 3d structures: A micro-architected materials database assisted strategy. *Comput Struct* 2021;255:106574.
- [22] Ferrer A, Cante JC, Hernández J, Oliver J. Two-scale topology optimization in computational material design: An integrated approach. *Int J Num Methods Eng* 2018;114(3):232–54.
- [23] Forest S. Mechanics of generalized continua: construction by homogenization. *Le J de Phys IV* 1998;8(PR4):39–48.
- [24] Forest S. Homogenization methods and mechanics of generalized continua—Part 2. *Theoret Appl Mech* 2002;28–29:113–44.
- [25] Forest S, Pradel F, Sab K. Asymptotic analysis of heterogeneous cosserat media. *Int J Solids Struct* 2001;38(26–27):4585–608.
- [26] Forest S, Sab K. Cosserat overall modeling of heterogeneous materials. *Mech Res Commun* 1998;25(4):449–54.
- [27] Gaynor AT, Meisel NA, Williams CB, Guest JK. Multiple-material topology optimization of compliant mechanisms created via polyjet three-dimensional printing. *J Manuf Sci Eng* 2014;136(6).
- [28] Gei M, Rovati M, Veber D. Effect of internal length scale on optimal topologies for cosserat continua. In: Bendsoe MP, Olhoff N, Sigmund O, editors. IUTAM symposium on topological design optimization of structures, machines and materials. Netherlands: Springer; 2006. p. 157–66.
- [29] Groen JP, Sigmund O. Homogenization-based topology optimization for high-resolution manufacturable microstructures. *Int J Numer Meth Eng* 2018;113(8):1148–63.
- [30] Jackowska-Strumillo L, Sokolowski J, Zochowski A. The topological derivative method in shape optimization. In: Proceedings of the 38th IEEE Conference on Decision and Control (Cat. No.99CH36304). vol. 1; 1999. p. 674–79.
- [31] Jang D, Meza LR, Greer F, Greer JR. Fabrication and deformation of three-dimensional hollow ceramic nanostructures. *Nat Mater* 2013;12(10):893–8.
- [32] Kato J, Yachi D, Kyoya T, Terada K. Micro-macro concurrent topology optimization for nonlinear solids with a decoupling multiscale analysis. *Int J Numer Meth Eng* 2018;113(8):1189–213.
- [33] Kouznetsova V, Geers MGD, Brekelmans WAM. Multi-scale constitutive modelling of heterogeneous materials with a gradient-enhanced computational homogenization scheme. *Int J Num Methods Eng* 2002;54(8):1235–60.
- [34] Kumar S, Tan S, Zheng L, Kochmann D. Inverse-designed spinoid metamaterials. *npj Comput Mater* 2020;6(1):73.
- [35] Lakes R. Experimental micro mechanics methods for conventional and negative poisson's ratio cellular solids as cosserat continua. *J Eng Mater Technol* 1991;113(1):148–55.
- [36] Lakes R. Materials with structural hierarchy. *Nature* 1993;361(6412):511–5.
- [37] Lakes R, Saha S. Cement line motion in bone. *Science* 1979;204(4392):501–3.
- [38] Li H, Luo Z, Gao L, Qin Q. Topology optimization for concurrent design of structures with multi-patch microstructures by level sets. *Comput Methods Appl Mech Eng* 2018;331:536–61.
- [39] Li L, Khandelwal K. Topology optimization of structures with length-scale effects using elasticity with microstructure theory. *Comput Struct* 2015;157:165–77.
- [40] Li X, Liu Q, Zhang J. A micro-macro homogenization approach for discrete particle assembly-cosserat continuum modeling of granular materials. *Int J Solids Struct* 2010;47(2):291–303.
- [41] Liebenstein S, Zaiser M. Determining cosserat constants of 2D cellular solids from beam models. *Mater Theory* 2018;2(1):1–20.
- [42] Liu S, Su W. Topology optimization of couple-stress material structures. *Struct Multidiscip Optim* 2010;40(1):319–27.
- [43] Lu Y, Wang Y. Structural optimization of metamaterials based on periodic surface modeling. *Comput Methods Appl Mech Eng* 2022;395:115057.
- [44] Mindlin RD. *Microstructure in linear elasticity*. Tech. rep., Columbia Univ New York Dept of Civil Engineering and Engineering Mechanics; 1963.
- [45] Mousanezhad D, Babaei S, Ebrahimi H, Ghosh R, Hamouda AS, Bertoldi K, et al. Hierarchical honeycomb auxetic metamaterials. *Sci Rep* 2015;5(1):1–8.
- [46] Otomori M, Yamada T, Izui K, Nishiwaki S. Matlab code for a level set-based topology optimization method using a reaction diffusion equation. *Struct Multidiscip Optim* 2015;51(5):1159–72.
- [47] Park HC, Lakes RS. Cosserat micromechanics of human bone: strain redistribution by a hydration sensitive constituent. *J Biomech* 1986;19(5):385–97.
- [48] Peng D, Merriman B, Osher S, Zhao H, Kang M. A pde-based fast local level set method. *J Comput Phys* 1999;155(2):410–38.
- [49] Pradel F, Sab K. Cosserat modelling of elastic periodic lattice structures. *Comptes Rendus de l'Académie des Sci-Series IIB-Mech-Phys-Astron* 1998;326(11):699–704.
- [50] Reis FD, Ganghoffer JF. Construction of micropolar continua from the asymptotic homogenization of beam lattices. *Comput Struct* 2012;112:354–63.
- [51] Ritchie RO. The conflicts between strength and toughness. *Nat Mater* 2011;10(11):817–22.
- [52] Rokoš O, Ameen MM, Peerlings RHJ, Geers MGD. Micromorphic computational homogenization for mechanical metamaterials with patterning fluctuation fields. *J Mech Phys Solids* 2019;123:119–37.
- [53] Rovati M, Veber D. Optimal topologies for micropolar solids. *Struct Multidiscip Optim* 2007;33(1):47–59.
- [54] Rueger Z, Lakes RS. Experimental cosserat elasticity in open-cell polymer foam. *Phil Mag* 2016;96(2):93–111.
- [55] Sab K, Pradel F. Homogenisation of periodic cosserat media. *Inte J Comput Appl Technol* 2009;34(1):60.
- [56] Sanders ED, Aguiló MA, Paulino GH. Multi-material continuum topology optimization with arbitrary volume and mass constraints. *Comput Methods Appl Mech Eng* 2018;340:798–823.
- [57] Sethian JA. *Level set methods, evolving interfaces in geometry, fluid mechanics computer vision, and materials sciences*, isbn-13: 978-0521572026. Cambridge Monographs on Applied and Computational Mathematics, 3; 1996.
- [58] Sigmund O. On the design of compliant mechanisms using topology optimization. *J Struct Mech* 1997;25(4):493–524.
- [59] Sigmund O. A 99 line topology optimization code written in matlab. *Struct Multidiscip Optim* 2001;21(2):120–7.
- [60] Sokolowski J, Zolesio J-P. Introduction to shape optimization. In: Introduction to shape optimization. Springer; 1992. p. 5–12.
- [61] Su W, Liu S. Topology design for maximization of fundamental frequency of couple-stress continuum. *Struct Multidiscip Optim* 2016;53(3):395–408.
- [62] Su W, Liu S. Size-dependent microstructure design for maximal fundamental frequencies of structures. *Struct Multidiscip Optim* 2020;62(2):543–57.
- [63] Toupin R. Elastic materials with couple-stresses. *Arch Rational Mech Anal* 1962;11(1):385–414.
- [64] Tozoni D, Dumas J, Jlanh Z, Panetta J, Panozzo D, Zorin D. A low-parametric rhombic microstructure family for irregular lattices. *ACM Trans Graphics (TOG)* 2020;39(4):101.
- [65] Veber D, Taliervo A. Topology optimization of three-dimensional non-centrosymmetric micropolar bodies. *Struct Multidiscip Optim* 2012;45(4):575–87.
- [66] Wang L, Cai Y, Liu D. Multiscale reliability-based topology optimization methodology for truss-like microstructures with unknown-but-bounded uncertainties. *Comput Methods Appl Mech Eng* 2018;339:358–88.
- [67] Watts S, Arrighi W, Kudo J, Tortorelli DA, White DA. Simple, accurate surrogate models of the elastic response of three-dimensional open truss micro-architectures with applications to multiscale topology design. *Struct Multidiscip Optim* 2019;60(4):1887–920.
- [68] Yamada T, Izui K, Nishiwaki S, Takezawa A. A topology optimization method based on the level set method incorporating a fictitious interface energy. *Comput Methods Appl Mech Eng* 2010;199(45–48):2876–91.
- [69] Yvonnet J, Auffray N, Monchiet V. Computational second-order homogenization of materials with effective anisotropic strain-gradient behavior. *Int J Solids Struct* 2020;191–192:434–48.
- [70] Zhang HW, Wang H, Chen BS, Xie ZQ. Analysis of Cosserat materials with Voronoi cell finite element method and parametric variational principle. *Comput Methods Appl Mech Eng* 2008;197(6–8):741–55.
- [71] Zhang XS, Paulino GH, Ramos Jr AS. Multimaterial topology optimization with multiple volume constraints: Combining the zpr update with a ground-structure algorithm to select a single material per overlapping set. *Int J Numer Meth Eng* 2018;114(10):1053–73.
- [72] Zheng J, Luo Z, Li H, Jiang C. Robust topology optimization for cellular composites with hybrid uncertainties. *Int J Numer Meth Eng* 2018;115(6):695–713.
- [73] Zheng L, Kumar S, Kochmann D. Data-driven topology optimization of spinoid metamaterials with seamlessly tunable anisotropy. *Comput Methods Appl Mech Eng* 2021;383:113894.
- [74] Zheng X, Smith W, Jackson J, Moran B, Cui H, Chen D, et al. Multiscale metallic metamaterials. *Nat Mater* 2016;15(10):1100–6.